Research Square

Preprints are preliminary reports that have not undergone peer review.
They should not be considered conclusive, used to inform clinical practice,
or referenced by the media as validated information.

Hierarchical Fe_3O_4@Ni-MOF on Nickel Foam for Enhanced Electrochemical Water Splitting and Supercapacitor Performance

Sameerah I. Al-Saeedi
Princess Nourah bint Abdulrahman University
Mahmoud A. Hefnawy
maahefnawy@gmail.com
Cairo University
Ghadah M. Al-Senani
Princess Nourah bint Abdulrahman University
Nada S. Al-Kadhi
Princess Nourah bint Abdulrahman University
Hoda A. Ahmed
Taibah University
Shymaa S. Medany
Cairo University

Research Article

Keywords: Fe_3O_4@Ni-MOF, Nickel foam, Water splitting, Supercapacitor, Electrocatalysis

Posted Date: November 9th, 2026

DOI: https://doi.org/10.21203/rs.3.rs-11310259/v1

License: This work is licensed under a Creative Commons Attribution 4.0 International License.
Read Full License

Additional Declarations: No competing interests reported.

Hierarchical Fe_3O_4@Ni-MOF on Nickel Foam for Enhanced Electrochemical Water Splitting and Supercapacitor Performance

Sameerah I. Al-Saeedi[1], Mahmoud A. Hefnawy[2*], Ghadah M. Al-Senani[1], Nada S. Al-Kadhi[1], Hoda A. Ahmed[3], Shymaa S. Medany[2*]

1- Department of Chemistry, College of Science, Princess Nourah bint Abdulrahman University, P.O. Box 84428, Riyadh 11671, Saudi Arabia.

2- Chemistry Department, Faculty of Science, Cairo University, 12613-Giza, Egypt.

3- Department of Chemistry, College of Science in Yanbu, Taibah University, Yanbu Governorate, Saudi Arabia

*Corresponding authors:

Mahmoud A. Hefnawy (maadel@cu.edu.eg; maahefnawy@gmail.com)

Shymaa S. Medany (shymaa@sci.cu.edu.eg; shymaasamir80@cu.edu.eg)

Abstract

The hierarchical Fe_3O_4@Ni-MOF composite was successfully fabricated directly on nickel foam and systematically characterized to confirm its crystal structure, morphology, chemical composition, porosity, and thermal stability. X-ray diffraction (XRD) analysis was employed to identify the crystalline phases and verify the successful formation of the Fe_3O_4 and Ni-MOF components, while scanning electron microscopy (SEM) and transmission electron microscopy (TEM) revealed the hierarchical morphology, surface features, and nanoscale structural characteristics of the composite. Fourier-transform infrared (FTIR) spectroscopy was used to identify the characteristic functional groups and chemical bonding interactions within the composite. Furthermore, Brunauer–Emmett–Teller (BET) analysis was conducted to evaluate the specific surface area and pore characteristics, while thermogravimetric analysis (TGA) was performed to assess thermal stability and decomposition behavior. The resulting Fe_3O_4@Ni-MOF/NF electrode exhibited enhanced electrochemical performance for water splitting, achieving HER and OER overpotentials of 120 mV and 250 mV, respectively, at 10 mA cm^{-2}, together with Tafel slopes of 94 and 109 mV dec^{-1}. In supercapacitor measurements, the electrode delivered a specific capacitance of 531 F g^{-1} at 0.5 A g^{-1} and retained 77.6% of its initial capacitance after 8000 cycles. The improved electrochemical behavior is attributed to the synergistic interaction between Fe_3O_4 and Ni-MOF, the hierarchical porous architecture, and the highly conductive three-dimensional nickel foam substrate, which collectively promote efficient electron transport, electrolyte accessibility, and rapid ion diffusion. Furthermore, the electrode's practical water-splitting capability was demonstrated using a two-electrode electrolytic cell powered by a DC power supply. The assembled cell exhibited an overall cell voltage (E_{cell}) of only 1.73 V at a current density of 10 mA cm^{-2}, confirming the feasibility of the Fe_3O_4@Ni-MOF/NF electrode for real-time electrochemical water-splitting applications. These results highlight the potential of the hierarchical Fe_3O_4@Ni-MOF/NF architecture as a multifunctional platform for efficient hydrogen production and electrochemical energy storage.

Keywords:

Fe_3O_4@Ni-MOF; Nickel foam; Water splitting; Supercapacitor; Electrocatalysis

1. Introduction

Energy is a fundamental requirement for economic growth, industrial development, technological progress, and the improvement of human quality of life[1,2]. As the global population continues to grow and industrialization expands, the demand for reliable and affordable energy is increasing significantly[3,4]. However, the continued reliance on fossil fuels to meet this growing demand has led to major environmental challenges, including greenhouse gas emissions, air pollution, climate change, and the depletion of finite natural resources[5,6]. In this context, renewable energy sources, such as solar, wind, hydropower, and biomass, have emerged as promising alternatives, as they provide cleaner, more sustainable energy while reducing dependence on conventional fuels[7–9]. Therefore, the development and integration of renewable energy technologies are essential for enhancing long-term energy security, minimizing environmental impacts, and supporting the transition toward a sustainable and low-carbon future[10,11].

Hydrogen energy has emerged as a promising alternative to conventional fossil fuels because of its high energy density, clean conversion, and potential to reduce greenhouse gas emissions[12,13]. Hydrogen can be produced from various sources and used in fuel cells to generate electricity, with water as the primary by-product of electrochemical conversion[14,15]. Furthermore, integrating hydrogen with renewable energy sources, particularly solar and wind, offers an attractive approach to storing excess renewable electricity and improving energy security[16,17].

Electrochemical capacitors, commonly known as supercapacitors, have attracted significant attention as advanced energy-storage devices due to their high-power density, rapid charge–discharge capability, excellent rate performance, and long cycling stability[18–20]. Unlike conventional batteries, supercapacitors can deliver and receive energy rapidly, making them particularly suitable for applications requiring high-power output and frequent charge–discharge cycles[21,22]. Their electrochemical performance strongly depends on the physicochemical properties and structure of the electrode materials, including transition-metal oxides, hydroxides, sulfides, and carbon-based materials[23,24]. Consequently, the development of low-cost, highly conductive, and structurally stable electrode materials is crucial for improving the energy density and overall performance of next-generation electrochemical capacitors[25,26].

Metal–organic frameworks (MOFs) are a class of porous crystalline materials composed of metal ions or clusters coordinated with organic linkers[27,28]. Their high surface area, tunable pore structures, and

diverse chemical functionality make them attractive materials for applications in energy storage, catalysis, gas adsorption, sensing, and environmental remediation[29,30].

John et al. developed an $Ag_2S/g\text{-}C_3N_4$ heterostructure integrated with boronized Ni-ZIF (B) for alkaline/saline water splitting and supercapacitor applications. The composite showed enhanced electrocatalytic activity, requiring overpotentials of 324 mV for OER and 78 mV for HER at 10 mA cm^{-2} in 1 M KOH, attributed to reduced charge-transfer resistance and increased electrochemically active surface area. It also achieved a high specific capacitance of 1076.6 F g^{-1} and demonstrated over 20 h of water-splitting stability with 86% capacitance retention, highlighting its potential as a multifunctional electrode for energy conversion and storage[31].

Magnetite (Fe_3O_4) is a naturally occurring iron oxide with a distinctive inverse spinel structure and attractive magnetic and electrochemical properties. Its relatively low cost, good chemical stability, and redox-active iron centers make it a promising material for applications in catalysis, environmental remediation, and energy-storage devices[32,33]. In particular, the reversible Fe^{2+}/Fe^{3+} redox chemistry of Fe_3O_4 can enhance charge-storage performance, making it an interesting electrode material for supercapacitors and other electrochemical energy technologies[34,35].

Al-Qahtani et al. successfully synthesized and characterized hybrid RGO/Fe_3O_4/Fe-MOF nanostructures for water splitting and electrochemical energy storage. The optimized Fe-MOF/RGO/Fe_3O_4 composite exhibited enhanced HER and OER activity, with overpotentials of 274 and 250 mV and Tafel slopes of 112 and 99 mV dec^{-1}, respectively, while maintaining stable catalytic performance for 6 h. In supercapacitor applications, the composite achieved a specific capacitance of 321 F g^{-1} at 0.5 A g^{-1}, retained 83% of its capacitance at 5 A g^{-1}, and preserved 91% of its capacitance after 10,000 cycles, demonstrating its potential as a multifunctional material for sustainable energy conversion and storage[36].

The novelty of this work lies in the rational design and fabrication of a binder-free Fe_3O_4@Ni-MOF heterostructure directly supported on nickel foam (NF) for dual applications in electrochemical water splitting and supercapacitor energy storage. The integration of Fe_3O_4 with Ni-MOF is expected to provide synergistic redox-active sites, enhanced interfacial charge transfer, and improved electrochemical accessibility, while the three-dimensional porous architecture of nickel foam facilitates efficient electrolyte penetration and rapid electron transport. The distinctive feature of the present strategy is the development of a single multifunctional electrode platform capable of addressing both efficient water-splitting reactions and high-performance capacitive energy storage, thereby

demonstrating the versatility of the Fe_3O_4@Ni-MOF/NF architecture for integrated energy-conversion and energy-storage applications.

2. Experimental section

2.1 Sonochemical synthesis of Ni-MOF/Ni Foam

Nickel foam (NF) pieces measuring 2 × 3 cm^2 and with an average thickness of 1.5 mm were used as the conductive substrate. Prior to synthesis, the NF was ultrasonically cleaned sequentially in acetone, ethanol, and deionized water for 15 min each, then dried at 60 °C. For the synthesis of Ni-MOF, 0.291 g of $Ni(NO_3)_2 \cdot 6H_2O$ and 0.166 g of terephthalic acid (H_2BDC) were dissolved in a mixed solvent consisting of 30 mL of N,N-dimethylformamide (DMF) and 10 mL of deionized water under magnetic stirring for 30 min. The pretreated Ni-foam substrate was fully immersed in the precursor solution, and the suspension was ultrasonically irradiated at 40 kHz and 150 W for 60 min while maintaining the temperature at approximately 50 °C. During sonication, acoustic cavitation facilitated rapid nucleation and in situ growth of the Ni-MOF crystals on the surface of the Ni foam, resulting in intimate contact between the MOF and conductive substrate. After sonication, the resulting Ni-MOF/NF was removed from the solution and washed three times with ethanol and deionized water to eliminate unreacted precursors and loosely attached particles. Finally, the electrode was dried at 60 °C for 12 h under vacuum before further characterization and electrochemical measurements. The resulting Ni-MOF/NF was used directly as a binder-free electrode.

2.2. Synthesis of Fe_3O_4 nanoparticles

The magnetite nanoparticles were synthesized through a facile chemical co-precipitation method using anhydrous $FeSO_4$ as the Fe^{2+} source. Briefly, 2.78 g of anhydrous $FeSO_4$ (20 mmol) and 10.81 g of $FeCl_3 \cdot 6H_2O$ (40 mmol) were separately dissolved in 50 mL of deoxygenated deionized water under continuous magnetic stirring. The two iron precursor solutions were subsequently mixed under a nitrogen atmosphere and stirred for 30 min to obtain a homogeneous solution. Then, 20 mL of 5 M NaOH solution was added dropwise under vigorous stirring until the pH reached approximately 10. The resulting suspension was maintained at 70 °C for 1 h under continuous stirring, during which a black precipitate corresponding to Fe_3O_4 nanoparticles was formed. The precipitate was magnetically separated and repeatedly washed with deionized water and ethanol to remove residual salts and unreacted species. Finally, the obtained Fe_3O_4 nanoparticles were dried under vacuum at 60 °C for 12 h

and gently ground to obtain a homogeneous powder. The synthesized Fe_3O_4 nanoparticles were subsequently used for the fabrication of the Fe_3O_4@Ni-MOF/NF.

2.3. Prepare the Fe_3O_4@Ni-MOF/NF

First, Fe_3O_4 nanoparticles were subsequently incorporated onto the preformed Ni-MOF/NF substrate through a facile sonochemical deposition process. Briefly, 50 mg of Fe_3O_4 nanoparticles was dispersed in 40 mL of ethanol/deionized water mixture (1:1, v/v) by ultrasonication for 30 min to obtain a homogeneous suspension. A previously prepared Ni-MOF/NF electrode, measuring 2 × 3 cm^2, was fully immersed in the Fe_3O_4 suspension and subjected to ultrasonic irradiation at 40 kHz and 150 W for 20 min. Ultrasonic cavitation facilitated the uniform dispersion and deposition of Fe_3O_4 nanoparticles across the Ni-MOF surface, thereby promoting intimate interfacial contact between Fe_3O_4 and the Ni-MOF/NF substrate. After sonication, the Fe_3O_4@Ni-MOF/Ni foam electrode was removed from the suspension and washed several times with ethanol and deionized water to eliminate weakly attached nanoparticles. The electrode was then dried under vacuum at 50 °C for 3 h.

2.4. Electrochemical measurement

Electrochemical measurements were performed using a PGSTAT128N Autolab potentiostat/galvanostat (Metrohm Autolab, The Netherlands) in a conventional three-electrode configuration. An Ag/AgCl electrode (3 M KCl) was used as the reference electrode, while a Pt wire served as the auxiliary (counter) electrode. Nickel foam (NF), Ni-MOF/NF, and Fe_3O_4@Ni-MOF/NF were directly employed as the working electrodes. The measured potentials were converted from the Ag/AgCl reference scale to the reversible hydrogen electrode (RHE) scale according to the following equation:

$$E_{RHE} = E_{Ag/AgCl} + 0.210 + 0.059 \text{ Log pH} \quad \textbf{(1)}$$

where ($E_{Ag/AgCl}$) is the experimentally measured potential (V), 0.210 V is the standard potential of an Ag/AgCl electrode containing 3 M KCl versus the standard hydrogen electrode (SHE) at 25 °C, and pH is the pH of the electrolyte.

The electrochemical active surface area calculated for different electrode surfaces (**Figure S1**) by the linear relationship between the current-density difference (ΔJ, mA cm^{-2}) and the scan rate (mV s^{-1}) for bare nickel foam (NF), Ni-MOF/NF, and Fe_3O_4@Ni-MOF/NF electrodes. The double-layer capacitance (C_{dl}) was determined from half the slope of the linear fit (Cdl = slope/2). The calculated (C_{dl}) values were 14.50, 21.65, and 25.10 mF cm^{-2} for NF, Ni-MOF/NF, and Fe_3O_4@Ni-MOF/NF, respectively. The progressively higher (C_{dl}) after incorporation of Ni-MOF and Fe_3O_4@Ni-MOF indicates an increased

electrochemically accessible surface area and enhanced electrode–electrolyte interfacial area. Assuming a specific capacitance (C_s) of 0.040 mF cm^{-2}, the corresponding electrochemically active surface areas (ECSA) were estimated to be 362.5, 541.25, and 627.5 cm^2, respectively. These results demonstrate that the Fe_3O_4@Ni-MOF/NF electrode provides the largest electrochemically accessible surface area among the investigated electrodes, which can contribute to its improved electrochemical performance.

3. Results and discussion

3.1. Analysis

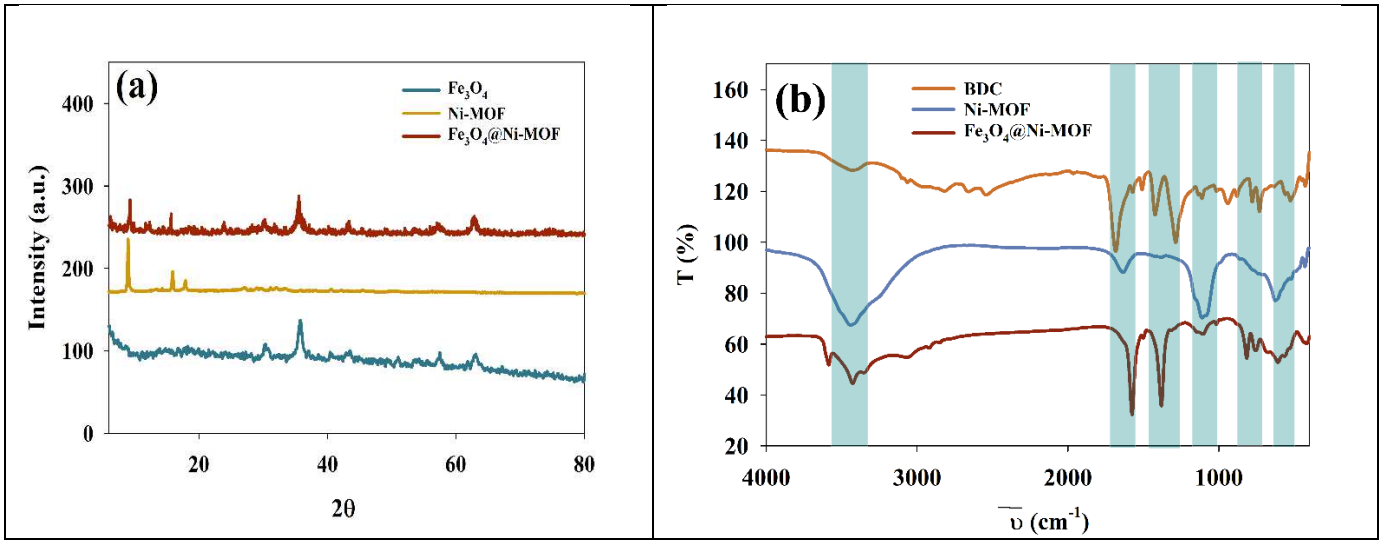
The X-ray diffraction (XRD) pattern of the synthesized Fe_3O_4, Ni-MOF, and Fe_3O_4@Ni-MOF are presented in **Figure 1a**. The diffraction pattern exhibits the characteristic reflections of crystalline Fe_3O_4, with prominent peaks located at 2θ = 30.1°, 35.5°, 43.1°, 53.5°, 57.0°, and 62.6°, which can be indexed to the (220), (311), (400), (422), (511), and (440) crystallographic planes, respectively[37]. These reflections are characteristic of the cubic inverse-spinel structure of magnetite (Fe_3O_4) and are consistent with the standard JCPDS/PDF card No. 19-0629. The absence of additional prominent diffraction peaks indicates that no detectable crystalline impurity phases are present in the prepared Fe_3O_4 sample. Thus, the XRD results confirm the successful formation of crystalline Fe_3O_4 with the characteristic cubic spinel structure. For Ni-MOF, The characteristic diffraction peaks observed at 2θ ≈ 8.6°, 11.8°, 17.1°, 20.7°, and 23.8° can be indexed to the (100), (010), (200), (101), and (020) crystallographic planes, respectively. These reflections are characteristic of the crystalline Ni-based MOF framework and are consistent with the reported crystal structure of Ni-MOF (CCDC No. 638866)[38]. The presence of the characteristic reflections without additional prominent crystalline peaks indicates the formation of the Ni-MOF phase under the employed synthesis conditions. The XRD pattern of Fe_3O_4@Ni-MOF shows the characteristic diffraction peaks of both components that confirm the loading of Fe_3O_4 on Ni-MOF surface.

The functional groups were investigated using FT-IR. **Figure 1b** presents the FTIR spectra of BDC, Ni-MOF, and Fe_3O_4@Ni-MOF. The BDC spectrum exhibits absorption bands at 3451, 1686, 1426, 1284, 1118, and 735 cm^{-1}. The band at 3451 cm^{-1} is assigned to O–H stretching, while the band at 1686 cm^{-1} corresponds to the C=O stretching vibration of the carboxylic acid group. The bands at 1426 and 1284 cm^{-1} are associated with aromatic and C–O vibrations, respectively, while the bands at 1118 and 735 cm^{-1} can be attributed to C–O and aromatic C–H vibrations. For Ni-MOF, the observed bands at 3434, 1635, 1109, and 626 cm^{-1} are assigned to O–H stretching, carboxylate-related vibrations, C–O

vibrations, and metal–oxygen (Ni–O) vibrations, respectively. The FTIR spectrum of Fe_3O_4@Ni-MOF shows bands at 3443, 3352, 1577, 1368, 1109, and 610 cm^{-1}. The bands at 3443 and 3352 cm^{-1} are associated with O–H stretching, whereas the bands at 1577 and 1368 cm^{-1} are related to carboxylate/aromatic vibrations. The band at 1109 cm^{-1} is attributed to C–O vibrations, while the absorption at 610 cm^{-1} is assigned to the Fe–O vibration of Fe_3O_4.

Figure 1c presents the thermogravimetric analysis (TGA) curves for BDC and the synthesized Ni-MOF, providing insight into their thermal weight-loss behavior. The BDC ligand exhibited a single major transition, with an almost complete weight loss of 99.96% between 241 and 429 °C, indicating substantial thermal decomposition within this temperature range. In comparison, the Ni-MOF displayed three distinct weight-loss stages. The first stage involved an 8.4% weight loss from 66 to 118 °C, which can be associated with the removal of weakly bound or adsorbed volatile species. The second stage showed a 26% weight loss between 125 and 334 °C, followed by a further 7% weight loss from 327 to 481 °C in the third stage. The latter two stages correspond to progressive thermal decomposition of the organic and framework components of the Ni-MOF. Overall, the TGA profile of Ni-MOF demonstrates a multistep thermal decomposition behavior, whereas BDC exhibits a single major decomposition transition.

Figure 1d shows the N_2 adsorption–desorption isotherm of Fe_3O_4@Ni-MOF. The material exhibits a BET specific surface area of 229.3 $m^2\ g^{-1}$, with a monolayer adsorption capacity of 52.68 cm^3(STP) g^{-1}. The total pore volume, estimated from the adsorption amount at $P/P_0 = 0.99$, was approximately 0.300 $cm^3\ g^{-1}$. Based on the BET surface area and total pore volume, the average pore diameter was calculated to be approximately 5.23 nm, indicating a predominantly mesoporous pore structure.



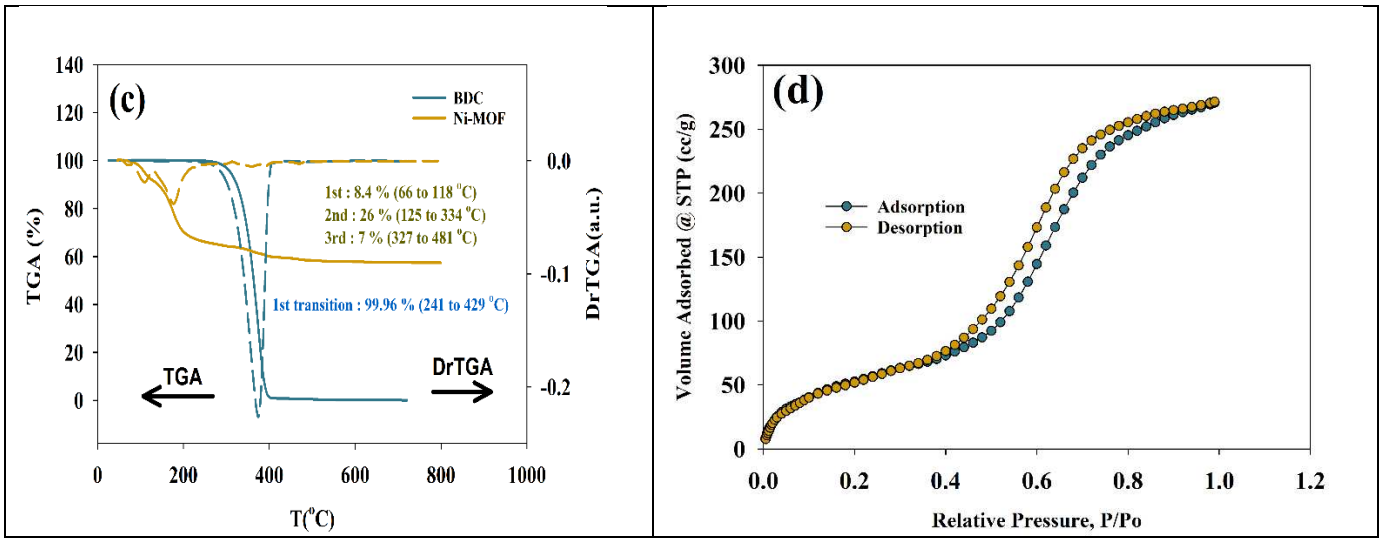


Figure 1. a) XRD**, b)** FT-IR, **c)** Thermal analysis, **d)** BET of the prepared nanomaterial.

The surface morphology of the Fe_3O_4@Ni-MOF/NF electrode was examined by SEM, as shown in **Figure. 2a and b**. At low magnification (**Figure 2a**), the Fe_3O_4@Ni-MOF composite appears uniformly distributed over the three-dimensional Ni foam substrate. The higher-magnification image (**Figure 2b**) reveals the nanosheet-like morphology of the Ni-MOF, with an average particle size of approximately 0.6 µm. Fe_3O_4 nanoparticles with an average size of approximately 36 nm are observed decorating the surfaces of the Ni-MOF nanosheets. This hierarchical morphology confirms the formation of the Fe_3O_4@Ni-MOF architecture and provides a textured electrode surface with nanoscale features. **Figure 2c** presents the SEM image of the Fe_3O_4@Ni-MOF/NF electrode after the HER stability test for 48 h. Compared with the pristine electrode, the surface morphology showed noticeable deterioration after prolonged electrochemical operation. The initially well-defined Ni-MOF nanosheet structure became less distinct, accompanied by changes in the surface texture and partial loss or rearrangement of the deposited material. These morphological changes indicate that prolonged HER operation affected the structural integrity of the Fe_3O_4@Ni-MOF/NF electrode. Additionally, the morphology of the catalysts was characterized by Transmitted electron microscopy. **Figure 2d** shows the TEM image of the synthesized Fe_3O_4 nanoparticles. The nanoparticles exhibit nanoscale morphology with relatively well-defined individual particles and some degree of aggregation. Based on the TEM analysis, the average particle size of the Fe_3O_4 nanoparticles was approximately 42 nm. **Figure 2e** presents the TEM image of the Fe_3O_4@Ni-MOF/NF composite, clearly showing the formation of the heterostructured architecture. The Ni-MOF forms sheet-like structures, while the Fe_3O_4 nanoparticles are distributed and decorated on

the surfaces of the Ni-MOF sheets. The intimate contact between the Fe_3O_4 nanoparticles and Ni-MOF sheets provides direct interfacial contact between the two components, confirming the successful formation of the Fe_3O_4@Ni-MOF composite structure. The elemental composition of the Fe_3O_4@Ni-MOF/NF composite was further investigated by energy-dispersive X-ray spectroscopy (EDX), as shown in **Figure 2f**. The EDX spectrum confirms the presence of Fe, Ni, O, and C elements, which are consistent with the successful integration of Fe_3O_4 and Ni-MOF onto the nickel foam substrate. The signals corresponding to Fe and O are attributed to the Fe_3O_4 component, while the Ni signal originates from both the Ni-MOF framework and the underlying nickel foam. The C signal is associated with the organic linker of the Ni-MOF. These elemental signals provide further evidence for the successful formation of the Fe_3O_4@Ni-MOF heterostructure on the nickel foam substrate.

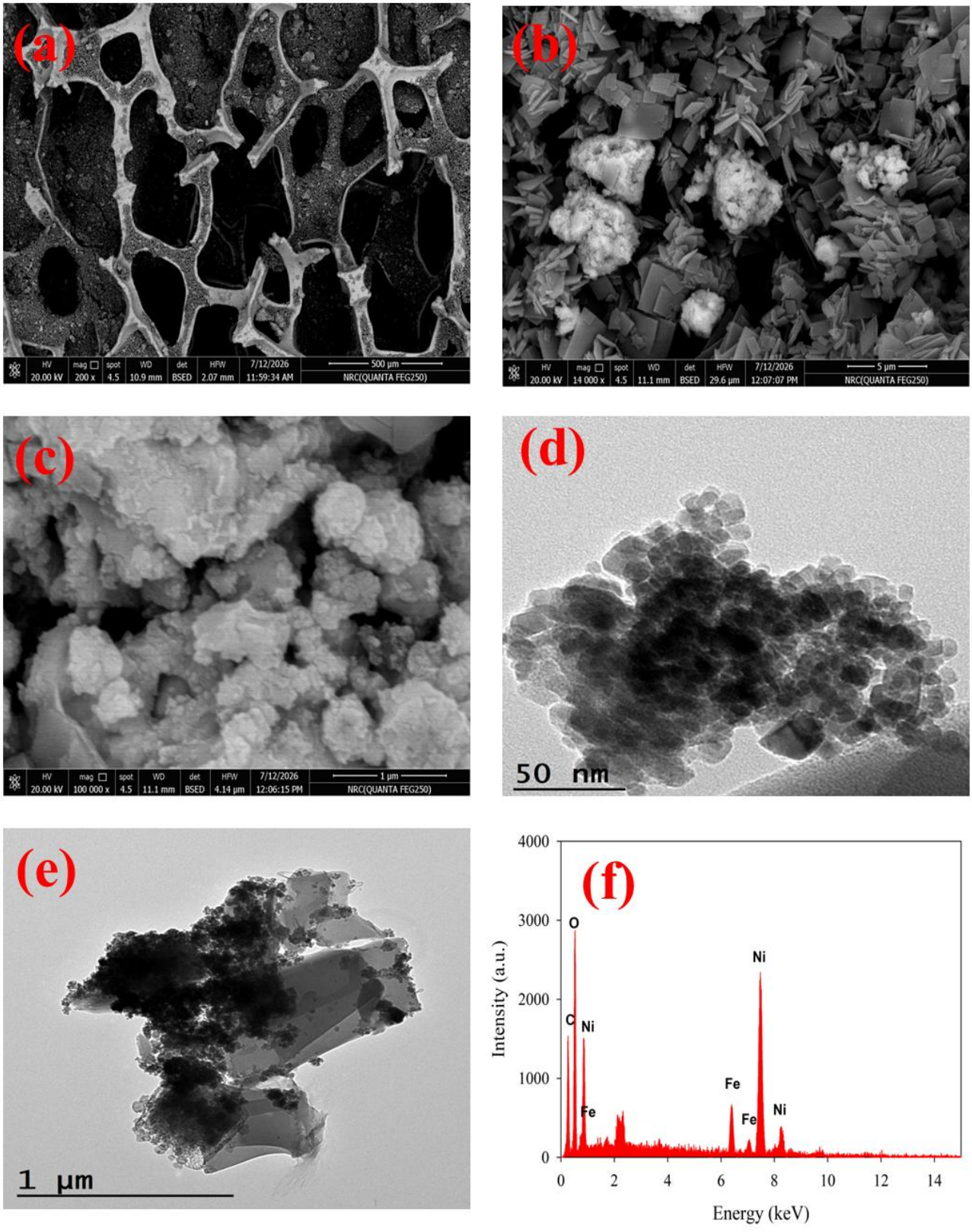

(a)
HV 20.00 kV
mag 200 x
spot 4.5
WD 10.9 mm
det BSED
HFW 2.07 mm
7/12/2026 11:59:34 AM
500 µm
NRC(QUANTA FEG250)
(b)
HV 20.00 kV
mag 14 000 x
spot 4.5
WD 11.1 mm
det BSED
HFW 29.6 µm
7/12/2026 12:07:07 PM
5 µm
NRC(QUANTA FEG250)
(c)
HV 20.00 kV
mag 100 000 x
spot 4.5
WD 11.1 mm
det BSED
HFW 4.14 µm
7/12/2026 12:06:15 PM
1 µm
NRC(QUANTA FEG250)
(d)
50 nm
(e)
1 µm
(f)
Intensity (a.u.)
Energy (keV)
O
C
Ni
Fe
Fe
Fe
Ni
Ni
0
1000
2000
3000
4000
0
2
4
6
8
10
12
14

Figure 2. (a-b) SEM of Fe_3O_4@Ni-MOF/NF**, c)** SEM of Fe_3O_4@Ni-MOF/NF after stability test**, d)** TEM of Fe_3O_4**, e)** TEM of Fe_3O_4@Ni-MOF, **(f)** EDX of Fe_3O_4@Ni-MOF.

3.2. Electrochemical performance of Fe_3O_4@Ni-MOF/NF

The electrochemical behavior of the different modified electrodes was investigated using cyclic voltammetry (CV) in an alkaline electrolyte. CV measurements were performed to evaluate the redox characteristics, electrochemical activity, and charge-transfer behavior of the prepared electrodes. The resulting CV profiles provide insight into the electrochemically active species and the contribution of the electrode modifications to the overall electrochemical performance.

For **Figure 3a**, CVs measurements of the bare NF electrode were recorded at different scan rates ranging from 5 to 50 mV s^{-1} in 1.0 M KOH over a potential window of 0–0.6 V vs. Ag/AgCl. The CV curves exhibit a distinct pair of redox peaks, indicating the reversible surface redox behavior of nickel species in the alkaline electrolyte. The anodic peak can be attributed to the oxidation of Ni(II) to Ni(III) (0.43 V vs. Ag/AgCl), while the corresponding cathodic peak is associated with the reverse reduction of Ni(III) to Ni(II) (0.24 V vs. Ag/AgCl). The presence of these redox features confirms that the Ni-based surface of NF actively participates in the electrochemical oxidation–reduction process. As the scan rate increases from 5 to 50 mV s^{-1}, the redox peak currents increase, indicating a robust electrochemical response of the NF electrode and its suitability as a conductive substrate for subsequent electrode modification.

Figure 3b presents the CV curves of the Ni-MOF/NF electrode recorded in 1.0 M KOH at different scan rates. Compared with the bare NF electrode, the incorporation of Ni-MOF results in a noticeable enhancement of the redox current response, indicating an increase in the electrochemically active surface area and improved accessibility of active sites. The anodic peak observed at approximately 0.35 V is attributed to the oxidation of Ni(II) to Ni(III), while the corresponding cathodic peak at approximately 0.26 V is associated with the reduction of Ni(III) back to Ni(II). Notably, the redox peaks of the Ni-MOF/NF electrode are shifted toward less positive potentials than those of pristine NF, indicating that the Ni(II)/Ni(III) redox process occurs at a more favorable potential and suggesting facilitated electrochemical kinetics upon Ni-MOF incorporation. The Ni-MOF coating also provides a porous structure that facilitates electrolyte penetration and promotes efficient charge transfer at the electrode/electrolyte interface. **Figure 3c** presents the CV curves of the Fe_3O_4@Ni-MOF/NF electrode recorded in 1.0 M KOH at different scan rates. The electrode exhibits two distinct redox couples, indicating the contribution of both Fe- and Ni-based redox processes to the overall electrochemical

response. The first redox couple is characterized by an anodic peak at approximately 0.21 V, which can be assigned to the oxidation of Fe_3O_4 to $Fe(OH)_3$, and a cathodic peak at approximately −0.048 V, corresponding to the reduction of $Fe(OH)_3$ to $Fe(OH)_2$. The second redox couple appears at higher potentials, with an anodic peak at approximately 0.35 V, attributed to the oxidation of the Ni-based species to $Ni(OH)_3$, and a cathodic peak at approximately 0.23 V, corresponding to the reduction of $Ni(OH)_3$ to $Ni(OH)_2$. The appearance of both redox couples confirms the electrochemical activity of the Fe_3O_4 and Ni-MOF components within the composite electrode. Furthermore, the progressive increase in redox peak currents with increasing scan rate indicates enhanced electrochemical response and efficient charge transfer in the Fe_3O_4@Ni-MOF/NF electrode.

For **Figure 3d**, the relationship between the logarithm of the peak current density and the logarithm of the scan rate was investigated to evaluate the electrochemical reaction kinetics and charge-storage mechanism of the different electrodes. The relationship was described by the power-law equation

$$i = av^b \qquad \textbf{(2)}$$

Where $i$is the peak current, $v$is the scan rate, $a$is a constant, and $b$is the slope of the linear $\log(i)$versus $\log(v)$plot. The obtained b-values were 0.53 for NF, 0.61 for Ni-MOF/NF, and 0.64 for Fe_3O_4@Ni-MOF/NF. Physically, the b-value provides information about the dominant electrochemical charge-storage or reaction kinetics: the value approaching 0.5 is generally associated with a diffusion-controlled process, whereas the value approaching 1.0 indicates a predominantly surface-controlled or capacitive process. Thus, the b-value of 0.53 for NF indicates mainly diffusion-controlled behavior, while the increase to 0.61 for Ni-MOF/NF suggests an enhanced contribution from surface-controlled processes. The higher b-value of 0.64 obtained for Fe_3O_4@Ni-MOF/NF indicates a further increase in the capacitive/surface-controlled contribution, reflecting faster ion-accessible electrochemical reactions and improved utilization of electrochemically active sites.

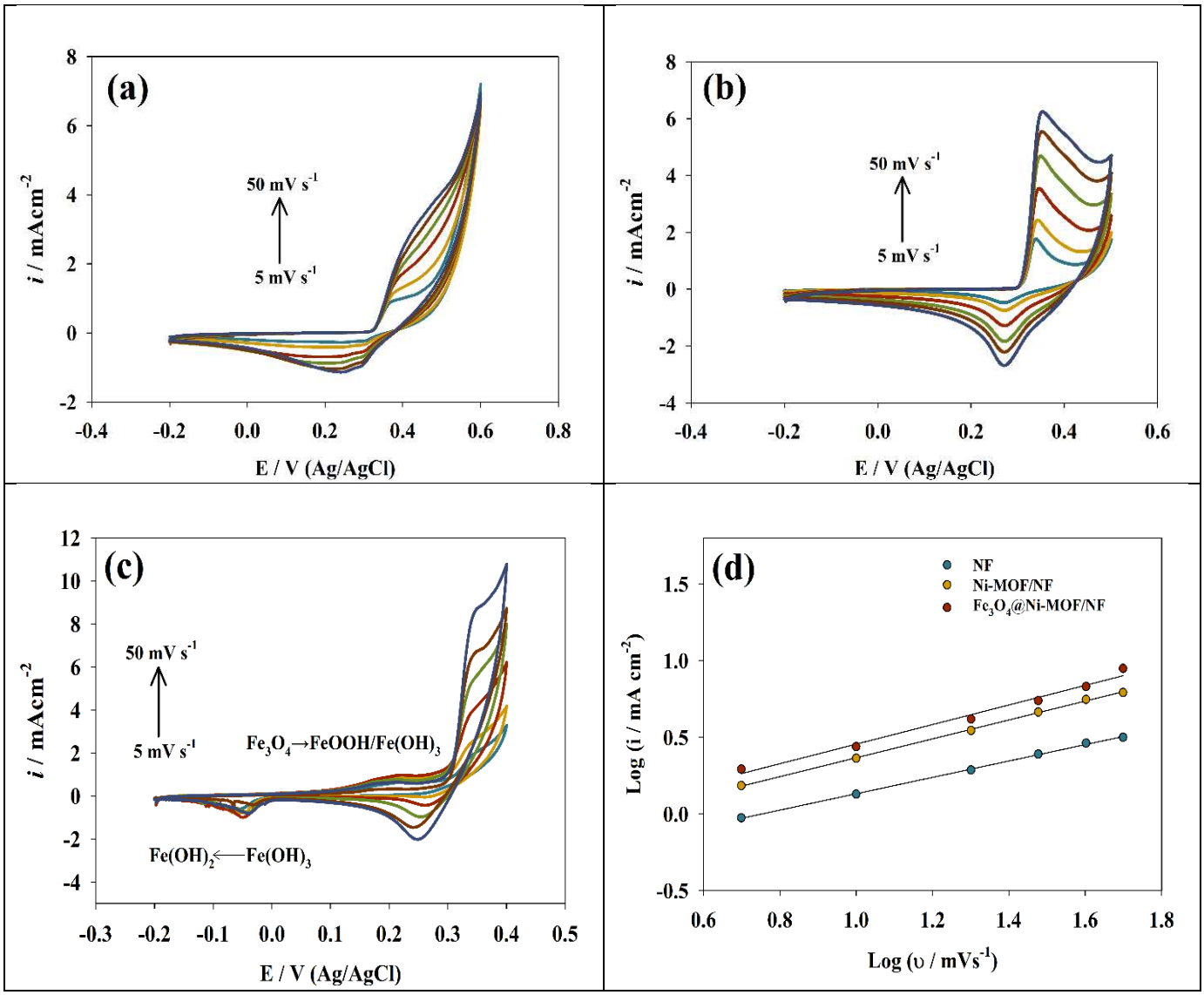


Figure 3. Cyclic voltammetry (CVs) curves of **(a)** bare Ni foam (NF), **(b)** Ni-MOF/NF, and **(c)** Fe_3O_4@Ni-MOF/NF electrodes in 1.0 M KOH at different scan rates. **(d)** Linear relationship between log(peak current) and log(scan rate) for NF, Ni-MOF/NF, and Fe_3O_4@Ni-MOF/NF electrodes.

Figure 4(a–c) presents the galvanostatic charge–discharge (GCD) curves of the bare NF, Ni-MOF/NF, and Fe_3O_4@Ni-MOF/NF electrodes, recorded in 1.0 M KOH electrolyte within a potential window of 0–0.4 V at current densities of 0.5, 1, 1.5, 2, and 2.5 A g^{-1}. As shown in **Figure 4(a)**, the bare NF exhibits nearly symmetric, quasi-triangular GCD profiles with very short discharge times at all applied current densities, indicating negligible faradaic contribution and a specific capacitance dominated by an electrical double-layer-like response from the nickel foam substrate itself. In contrast, the Ni-MOF/NF

electrode (**Figure 4b**) displays GCD curves with a distinct non-linear, plateau-like shape rather than a perfect triangle, which is a signature of reversible faradaic redox reactions associated with the Ni^{2+}/Ni^{3+} transitions in the MOF framework. The discharge time is noticeably prolonged relative to bare NF at every current density, confirming that the growth of the Ni-MOF significantly enhances the charge-storage capacity of the electrode. The most pronounced change is observed for the Fe_3O_4@Ni-MOF/NF composite electrode (**Figure 4c**), whose GCD curves show even longer discharge durations along with well-defined voltage plateaus, reflecting a stronger and more efficient battery-type (pseudocapacitive) redox behavior. This improvement can be attributed to the synergistic coupling between Fe_3O_4 nanoparticles and the Ni-MOF matrix, which increases the number of accessible active sites, improves electrical conductivity, and facilitates faster electron/ion transport during the charge–discharge process.

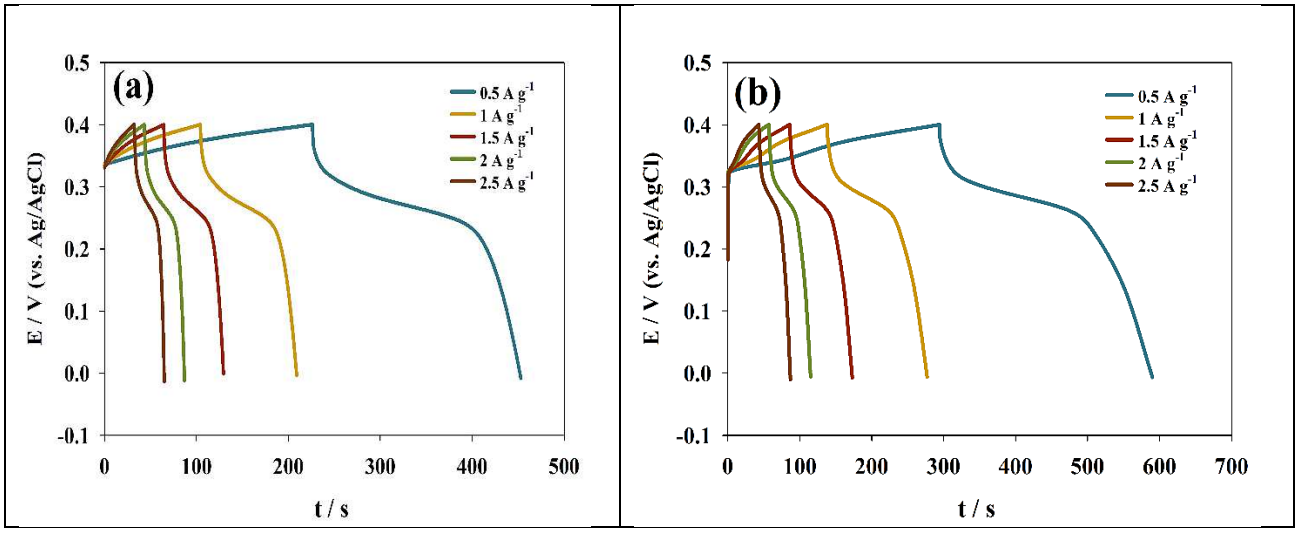
Figure 4(d) illustrates the variation of specific capacitance as a function of current density (0.5–2.5 A g^{-1}) for the NF, Ni-MOF/NF, and Fe_3O_4@Ni-MOF/NF electrodes, as calculated from their respective GCD discharge curves. As expected, all three electrodes exhibit a gradual decline in specific capacitance with increasing current density, which is a common feature of pseudocapacitive and battery-type electrode materials, arising from limited ion diffusion and insufficient time for electrolyte ions to access the inner active sites at higher charge–discharge rates. The bare NF electrode shows the lowest specific capacitance values across the entire current range, decreasing from 283 F g^{-1} at 0.5 A g^{-1} to 201 F g^{-1} at 2.5 A g^{-1}, consistent with its limited electroactive surface area. The Ni-MOF/NF electrode demonstrates a marked improvement, with specific capacitance decreasing from 368 F g^{-1} to 268 F g^{-1} over the same current range, reflecting the additional pseudocapacitive contribution from the redox-active Ni-MOF framework. Notably, the Fe_3O_4@Ni-MOF/NF composite electrode delivers the highest specific capacitance at all current densities, decreasing from 531 F g^{-1} at 0.5 A g^{-1} to 410 F g^{-1} at 2.5 A g^{-1}, which is significantly superior to both the bare NF and Ni-MOF/NF electrodes. The rate capability of each electrode, defined as the percentage retention of specific capacitance at the highest current density (2.5 A g^{-1}) relative to the lowest current density (0.5 A g^{-1}), was calculated using the following relation:

$$Rate\ capability\ (\%) = \frac{C_s\ at\ 2.5\ A.g^{-1}}{C_s at\ 0.5\ A.g^{-1}} \times 100 \qquad \textbf{(3)}$$

Accordingly, the bare NF electrode exhibits a rate capability of 71.0% (201/283 × 100), the Ni-MOF/NF electrode shows a rate capability of 72.8% (268/368 × 100), while the Fe_3O_4@Ni-MOF/NF composite electrode achieves the highest rate capability of 77.2% (410/531 × 100). This trend clearly indicates that the incorporation of Fe_3O_4 nanoparticles into the Ni-MOF framework not only enhances the overall

specific capacitance but also improves the rate capability of the electrode, suggesting faster ion/electron transport kinetics and better structural stability of the Fe_3O_4@Ni-MOF/NF composite under high current loading conditions. These results confirm the superior electrochemical performance and charge-storage efficiency of the Fe_3O_4@Ni-MOF/NF electrode compared to the pristine Ni-MOF/NF and bare NF electrodes.

Figure 4e shows the cycling stability of the Fe_3O_4@Ni-MOF/NF electrode during 8000 consecutive galvanostatic charge–discharge (GCD) cycles in 1.0 M KOH at a current density of 5 A g^{-1}. The electrode retains 77.6% of its initial specific capacitance after 8000 cycles, indicating that a substantial proportion of its initial charge-storage performance is maintained during prolonged cycling. The gradual decrease in capacitance observed during repeated cycling reflects a loss of electrochemical performance with continued operation. Nevertheless, the relatively high capacitance retention indicates good cycling stability of the Fe_3O_4@Ni-MOF/NF electrode under the experimental conditions.



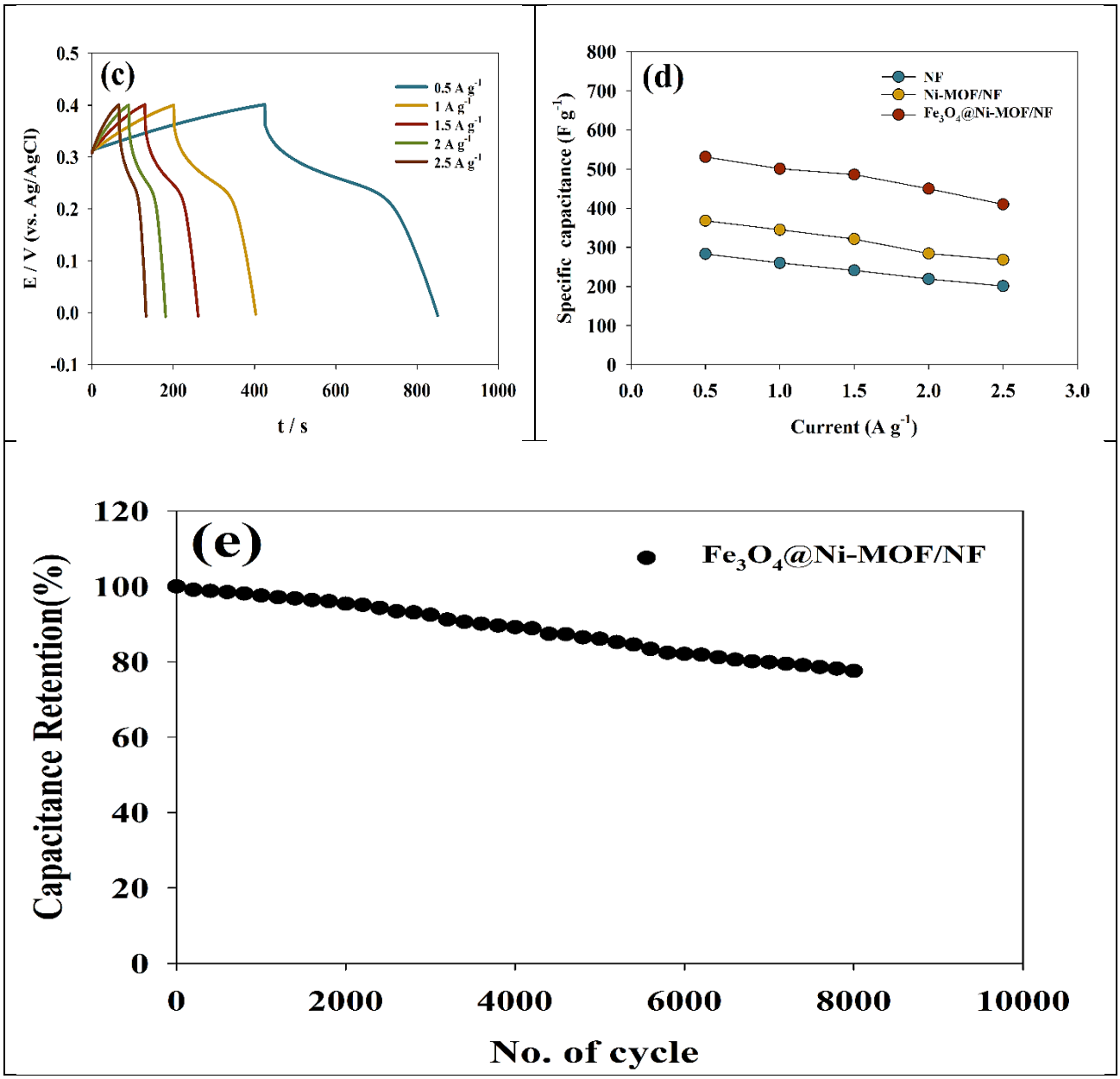


Figure 4. Galvanostatic charge–discharge (GCD) profiles of **(a)** NF, **(b)** Ni-MOF/NF, and **(c)** Fe_3O_4@Ni-MOF/NF electrodes, **(d)** Variation of specific capacitance as a function of current density (0.5–2.5 A g^{-1}) for different surfaces, and **(e)** Cycling stability of the Fe_3O_4@Ni-MOF/NF electrode during 8000 consecutive GCD cycles in 1.0 M KOH at a current density of 5 A g^{-1}.

3.3. Electrochemical hydrogen reaction

The hydrogen evolution reaction (HER) is a crucial half-reaction in water electrolysis and significantly contributes to the sustainable production of green hydrogen. Therefore, it is essential to develop efficient, durable HER electrocatalysts that operate at low overpotential, as this will help reduce the energy consumption associated with electrochemical hydrogen production.

The HER performance of the pristine Ni foam (NF), Ni-MOF/NF, and Fe_3O_4@Ni-MOF/NF electrodes was evaluated using linear sweep voltammetry (LSV) at a scan rate of 10 mV s^{-1} in 1.0 M KOH. As shown in **Figure 5a**, the polarization curves reveal a clear enhancement in the electrocatalytic activity following electrode modification. The bare NF electrode exhibited an overpotential (η_{10}) of 310 mV at a current density of 10 mA cm^{-2}, whereas the Ni-MOF/NF electrode required only 150 mV. Notably, the Fe_3O_4@Ni-MOF/NF electrode demonstrated the lowest η_{10} of 120 mV, indicating its superior HER catalytic activity among the investigated electrodes. The enhanced performance of Fe_3O_4@Ni-MOF/NF can be associated with the synergistic interaction between Fe_3O_4 and Ni-MOF, which may promote charge transfer and increase the accessibility of catalytically active sites. Thus, the HER activity follows the order NF (310 mV) > Ni-MOF/NF (150 mV) > Fe_3O_4@Ni-MOF/NF (120 mV), confirming the beneficial effect of Fe_3O_4 incorporation into the Ni-MOF/NF architecture.

The overall HER in alkaline medium over Fe_3O_4@Ni-MOF is expressed as:

$$Fe_3O_4@\text{Ni-MOF} + H_2O + e^- \rightarrow Fe_3O_4@\text{Ni-MOF}{-}H^* + OH^- \quad \textbf{(4)} \quad \text{(Volmer step)}$$

$$Fe_3O_4@\text{Ni-MOF} - H^* + H_2O + e^- \rightarrow Fe_3O_4@\text{Ni-MOF} + H_2 + OH^- \quad \textbf{(5)} \quad \text{(Heyrovsky step)}$$

$$2Fe_3O_4@\text{Ni-MOF}{-}H^* \rightarrow 2Fe_3O_4@\text{Ni-MOF} + H_2 \quad \textbf{(6)} \quad \text{(Tafel step)}$$

Overall, HER reaction in alkaline medium:

$$2H_2O + 2e^- \rightarrow H_2 + 2OH^- \quad \textbf{(7)}$$

The HER kinetics of the prepared electrodes were further investigated through Tafel analysis, as presented in **Figure 5b**. The Tafel slopes were obtained from the linear region of the polarization curves using the Tafel equation:

$$\eta = b \log(j) + a \quad \textbf{(8)}$$

Where η is the overpotential, j is the current density, b is the Tafel slope, and a is the intercept. The pristine NF electrode exhibited a relatively high Tafel slope of 126 mV dec^{-1}, indicating slower HER kinetics. Upon incorporation of Ni-MOF, the Tafel slope decreased to 102 mV dec^{-1}, demonstrating improved reaction kinetics. Remarkably, the Fe_3O_4@Ni-MOF/NF electrode exhibited the lowest Tafel

slope of only 94 mV dec^{-1}, confirming its more favorable HER kinetics compared with the other electrodes. The decrease in Tafel slope can be associated with enhanced electron-transfer processes and improved accessibility of catalytic active sites resulting from the incorporation of Ni-MOF and Fe_3O_4.

For **Figure 5c**, electrochemical impedance spectroscopy (EIS) measurements were conducted to investigate the interfacial charge-transfer characteristics of the investigated electrodes toward the HER. The experimental impedance spectra were fitted using the equivalent electrical circuit presented as the inset of **Figure 5c**, which consists of the solution resistance (Rc), constant phase elements (CPE1 and CPE2), and charge-transfer resistances (R1 and R2). The corresponding fitting parameters, including the resistance and CPE values with their respective Y_0 and N parameters, are summarized in **Table 1**. The good agreement between the experimental and fitted spectra confirms the suitability of the proposed equivalent circuit for describing the electrochemical behavior of the modified electrodes.

The long-term electrochemical stability of the prepared electrodes toward the HER was evaluated by chronoamperometric measurements at a constant potential in 1.0 M KOH, as shown in **Figure 5d**. The stability tests were conducted for 48 h to assess the electrodes' ability to maintain catalytic activity during prolonged electrolysis. The pristine NF electrode retained approximately 67% of its initial current after 48 h, while the Ni-MOF/NF electrode showed an improved current retention of 71%. Notably, the Fe_3O_4@Ni-MOF/NF electrode exhibited the highest current retention, 73%, after 48 h, indicating comparatively enhanced long-term stability. The improved durability of Fe_3O_4@Ni-MOF/NF can be attributed to the stable composite architecture and the interaction between Fe_3O_4 and Ni-MOF, which may help maintain the accessibility and integrity of the catalytic active sites during prolonged electrochemical operation. These results demonstrate that the Fe_3O_4@Ni-MOF/NF electrode maintains a relatively stable HER response over extended operation in alkaline electrolyte. A comparison of Fe_3O_4@Ni-MOF/NF and other surfaces for HER is reported in **Table 2.**

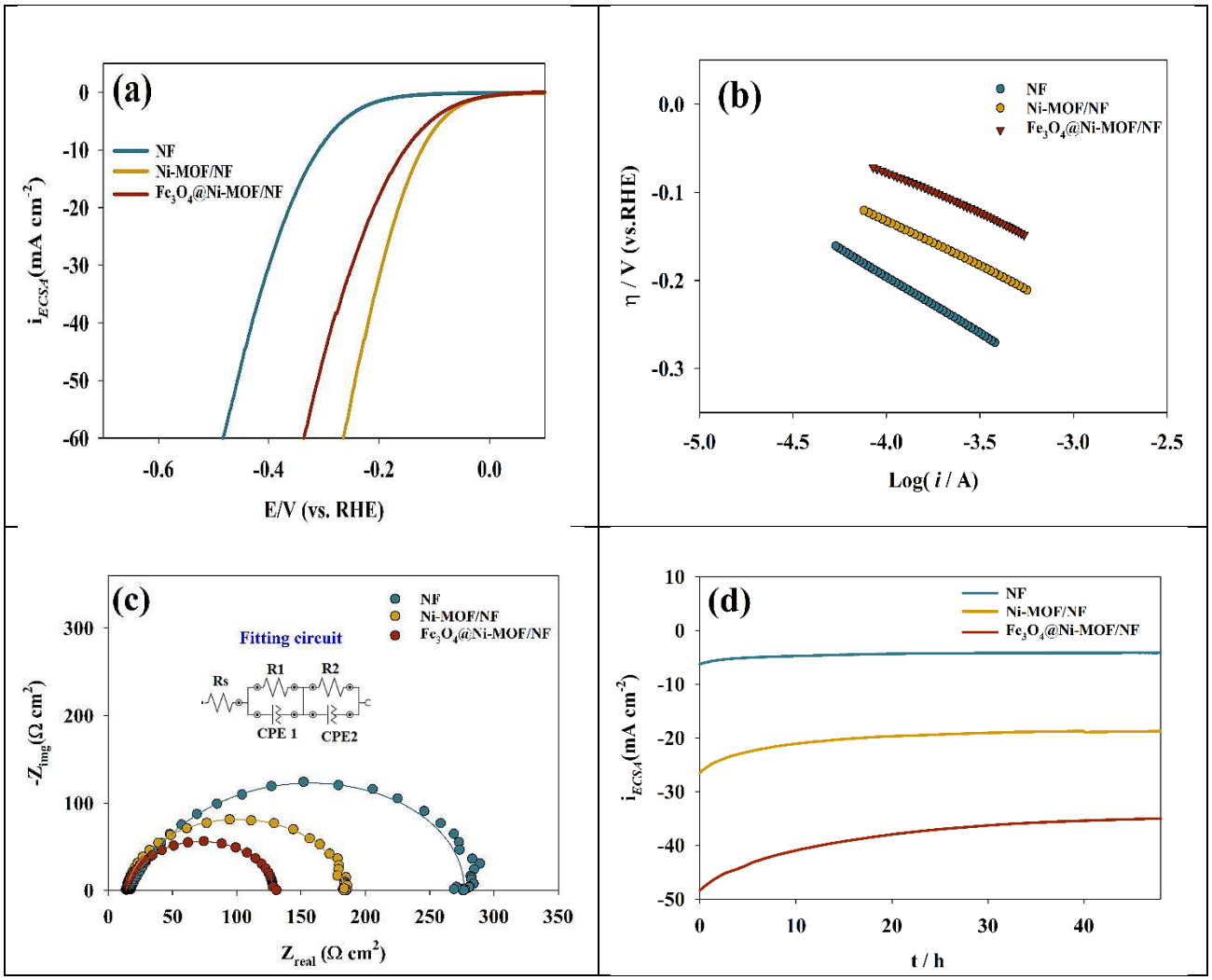


Figure 5. HER electrocatalytic performance of NF, Ni-MOF/NF, and Fe_3O_4@Ni-MOF/NF electrodes in 1.0 M KOH: (a) LSV polarization curves recorded at a scan rate of 10 mV s^{-1}, (b) corresponding Tafel plots, (c) Nyquist plots of the prepared electrodes, and (d) long-term durability test conducted for 48 h.

Table 1. Fitting parameters for HER.

Electrode	R_c(Ω cm^2)	R_1(Ω cm^2)	CPE1		R_2(Ω cm^2)	CPE2	
			Y0	N		Y0	N
NF	14.1	26	0.0001467	0.7346	276	0.0002894	0.8163
Ni-MOF/NF	13.4	21	0.0002952	0.8411	184	0.0004511	0.8507
Fe_3O_4@Ni-MOF/NF	13.1	18	0.0003147	0.8387	128	0.0005087	0.8429

Table 2. Comparison of different surfaces for HER

Materials	Electrolyte concentration	η10 / mV	Tafel slope / mV dec^{-1}	References

2D Co-BDC/MoS2	1.0 M KOH	248	86	[39]
Co-BHT	0.1 $NaClO_4$	185	88	[40]
PAAQ-CuO/GC	1.0 M NaOH	146	136	[41]
Fe(OH)x@Cu-MOF NBs	1.0 M KOH	112	76	[42]
ZMCO@PANI-NW	1.0 M KOH	296	84	[43]
Fe_3O_4@Ni-MOF/NF	1.0 M KOH	120	94	This work

3.4. Study of oxygen evolution reaction

The OER is a critical anodic process in water electrolysis and plays an essential role in the sustainable production of hydrogen. However, the slow reaction kinetics and high energy demand of OER highlight the need for efficient and durable electrocatalysts. These catalysts aim to lower the required overpotential and enhance overall energy efficiency.

For **Figure 6a**, the OER electrocatalytic performance of the prepared electrodes was evaluated by linear sweep voltammetry (LSV) in 1.0 M KOH at a scan rate of 10 mV s^{-1}. The overpotential required to achieve a current density of 10 mA cm^{-2} (η_{10}) was 410 mV for bare NF, which decreased to 330 mV for Ni-MOF/NF. Notably, the Fe_3O_4@Ni-MOF/NF electrode exhibited the lowest η_{10} of 250 mV, indicating substantially enhanced OER activity compared with both NF and Ni-MOF/NF. The lower overpotential demonstrates that the Fe_3O_4@Ni-MOF modification facilitates the OER process and promotes more efficient catalytic reactions, which can be associated with the synergistic interaction between Fe_3O_4 and the Ni-MOF framework and the improved accessibility of active catalytic sites.

For the OER in alkaline electrolyte, the mechanism on the Fe_3O_4@Ni-MOF/NF catalyst can be described by the following surface-adsorbed intermediates:

$$Fe_3O_4@Ni\text{-}MOF + OH^- \rightarrow Fe_3O_4@Ni\text{-}MOF\text{–}OH + e^- \quad \textbf{(9)}$$

$$Fe_3O_4@Ni\text{-}MOF\text{–}OH + OH^- \rightarrow Fe_3O_4@Ni\text{-}MOF\text{–}O + H_2O + e^- \quad \textbf{(10)}$$

$$Fe_3O_4@Ni\text{-}MOF\text{–}O + OH^- \rightarrow Fe_3O_4@Ni\text{-}MOF\text{–}OOH + e^- \quad \textbf{(11)}$$

$$Fe_3O_4@Ni\text{-}MOF\text{–}OOH + OH^- \rightarrow Fe_3O_4@Ni\text{-}MOF + O_2 + H_2O + e^- \quad \textbf{(12)}$$

The overall OER process can therefore be expressed as:

$$4OH^- \rightarrow O_2 + 2H_2O + 4e^- \quad \textbf{(13)}$$

In **Figure 6b,** Tafel plots were used to evaluate OER kinetics and to compare the intrinsic electrocatalytic activity of the prepared electrodes. The calculated Tafel slopes were 164 mV dec^{-1} for NF, 117 mV dec^{-1} for Ni-MOF/NF, and 109 mV dec^{-1} for Fe_3O_4@Ni-MOF/NF. The progressive decrease in Tafel slope after modification indicates faster OER reaction kinetics and more favorable electron-transfer processes compared with the bare NF electrode. In particular, the Fe_3O_4@Ni-MOF/NF electrode exhibited the lowest Tafel slope (109 mV dec^{-1}), demonstrating its improved OER kinetics, which can be attributed to the synergistic interaction between Fe_3O_4 and Ni-MOF and the resulting enhancement of the electrochemically active catalytic surface.

For **Figure 6c**, electrochemical impedance spectroscopy (EIS) measurements were performed to investigate the interfacial charge-transfer characteristics of the investigated electrodes toward the OER. The experimental impedance spectra were fitted using the equivalent electrical circuit shown in the inset of **Figure 6c**, consisting of the solution resistance (Rc), constant phase elements (CPE1 and CPE2), and the corresponding resistance components (R1 and R2). The fitting parameters obtained from the EIS analysis are summarized in **Table 3**. The bare NF electrode exhibited an R2 value of 455 Ω cm^2, which decreased to 386 Ω cm^2 for Ni-MOF/NF and further decreased to 248 Ω cm^2 for Fe_3O_4@Ni-MOF/NF. Similarly, R1 increased from 24 Ω cm^2 for NF to 287 Ω cm^2 for Ni-MOF/NF and then decreased to 159 Ω cm^2 for Fe_3O_4@Ni-MOF/NF. The CPE parameters also varied following electrode modification, with the Y_0 and N values reflecting changes in the interfacial electrochemical characteristics. Overall, the lower R2 value obtained for Fe_3O_4@Ni-MOF/NF indicates more favorable interfacial charge-transfer kinetics during OER compared with the other investigated electrodes.

For **Figure 6d**, the long-term durability of the electrodes toward the OER was evaluated by continuous electrolysis for 48 h in 1.0 M KOH. The current retention after the stability test was 63% for bare NF, 67% for Ni-MOF/NF, and 71% for Fe_3O_4@Ni-MOF/NF. The Fe_3O_4@Ni-MOF/NF electrode exhibited the highest current retention, indicating improved long-term operational stability compared with the unmodified NF and Ni-MOF/NF electrodes. The enhanced durability can be attributed to the robust integration of Fe_3O_4 and Ni-MOF with the Ni foam substrate, which helps maintain the catalytic structure and active sites during prolonged OER operation. A comparison of Fe_3O_4@Ni-MOF/NF and other surfaces for OER is reported in **Table 4.**

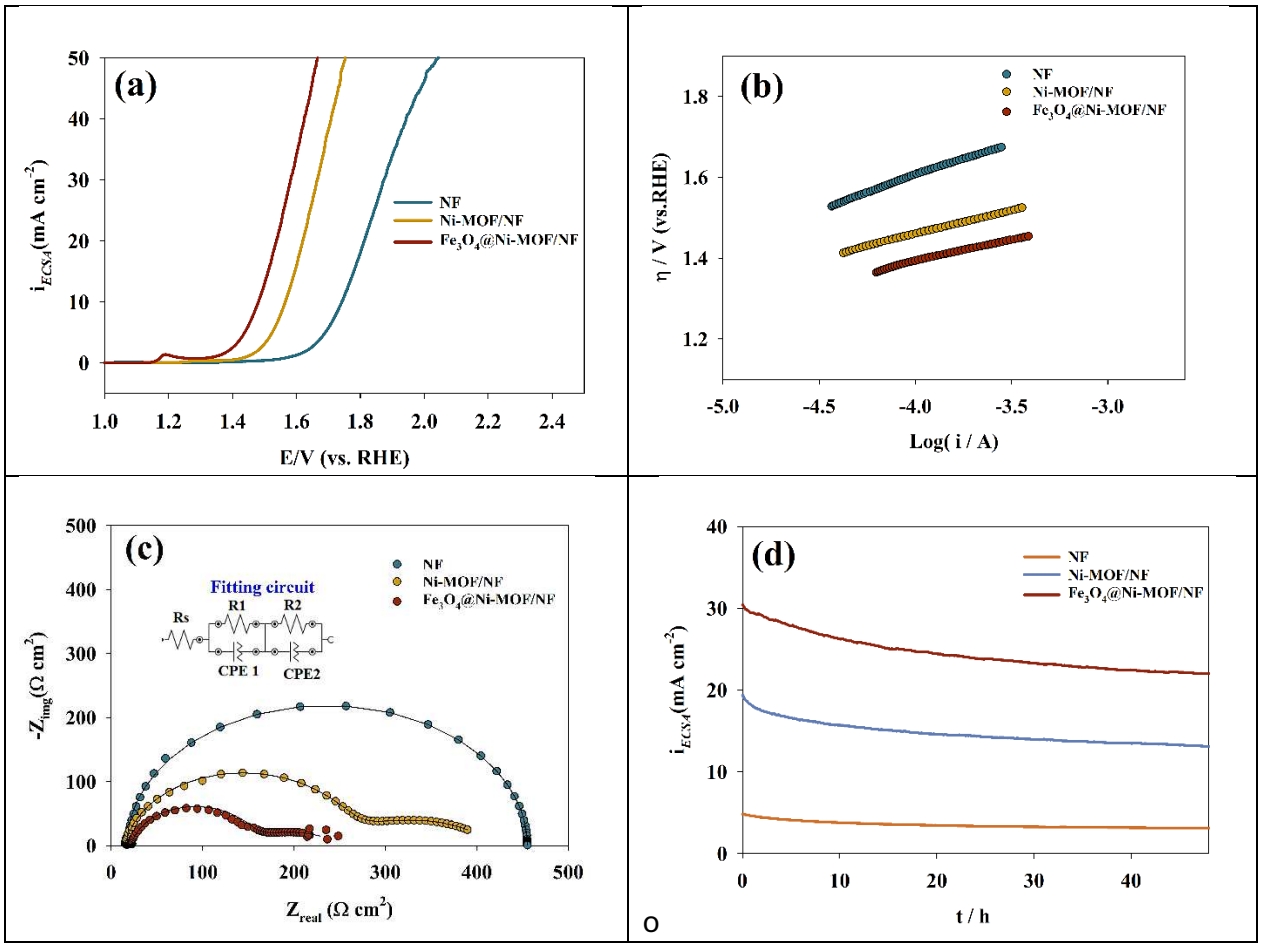


Figure 6. OER electrocatalytic performance of NF, Ni-MOF/NF, and Fe_3O_4@Ni-MOF/NF electrodes in 1.0 M KOH: (a) LSV polarization curves recorded at a scan rate of 10 mV s^{-1}, (b) corresponding Tafel plots, (c) Nyquist plots of the prepared electrodes, and (d) long-term durability test conducted for 48 h.

Table 3. Fitting parameters for OER.

Electrode	R_c(Ω cm^2)	R_1(Ω cm^2)	CPE1		R_2(Ω cm^2)	CPE2	
			Y0	N		Y0	N
NF	18	24	0.00003447	0.671	455	0.0000610	0.862
Ni-MOF/NF	15	287	0.00005399	0.851	386	0.0000638	0.886
Fe3O4@Ni-MOF/NF	16	159	0.00006524	0.814	248	0.0000729	0.934

Table 4. Comparison of different surfaces for OER

Materials	Electrolyte concentration	η10 / mV	Tafel slope / mV dec^{-1}	References

NiFe-MOF array / Ni foam	0.1 M KOH	240	34	[44]
Graphene-nanoplatelets-supported NiFe-MOF	1.0 M KOH	220	51	[45]
Ag@Ni-Cr-MOF/CF	1.0 M KOH	200	68	[46]
Ni–Cr-MOF/CNT/NF	1.0 M KOH	310	146	[29]
$Ni_{10}Fe$-BTC	1.0 M KOH	346	47	[47]
Fe_3O_4@Ni-MOF/NF	1.0 M KOH	250	109	This work

3.5. Two-electrode water splitting

To evaluate the water-splitting performance, a two-electrode electrochemical configuration was employed, using two identical, symmetrically positioned electrodes with an active geometric area of 1 × 1 cm^2. The electrodes were immersed in an aqueous 1.0 M KOH electrolyte and connected directly to a DC power supply. A constant or progressively varied DC voltage was applied across the two electrodes to induce water electrolysis. The resulting current was recorded at each applied voltage to assess the electrochemical response and overall water-splitting activity of the electrode material. The electrolysis process was conducted under ambient conditions, and the applied voltage–current response was used to evaluate the performance and operational stability of the assembled two-electrode water-splitting system.

Figure 7a shows the raw constant-current data obtained for the different modified electrodes. The corresponding cell voltage was recorded over time under identical operating conditions, enabling direct comparison of the electrochemical water-splitting performance and stability of the investigated electrodes. Raw data for the constant current mode of DC-Power supply using two electrode Fe3O4@Ni-MOF/NF at different current ranges is presented in Figure **S2**.

Figure 7b compares the cell voltage (E_{cell}) of the different electrodes at a current of 10 mA. NF exhibited an E_{cell} of 2.34 V, which decreased to 2.26 V for Ni-MOF/NF and further to 1.73 V for Fe_3O_4@Ni-MOF/NF. The markedly lower E_{cell} of Fe_3O_4@Ni-MOF/NF indicates its enhanced electrocatalytic performance and reduced energy requirement for water splitting. **Figure 7c** illustrates the relationship between the applied current and cell voltage (E_{cell}) for the Fe_3O_4@Ni-MOF/NF electrode. The E_{cell} increased progressively from 1.73 V at 10 mA to 4.35 V at 80 mA, indicating

increasing polarization with increasing current. The electrode maintained a relatively low cell voltage at lower current densities, demonstrating favorable water-splitting performance.

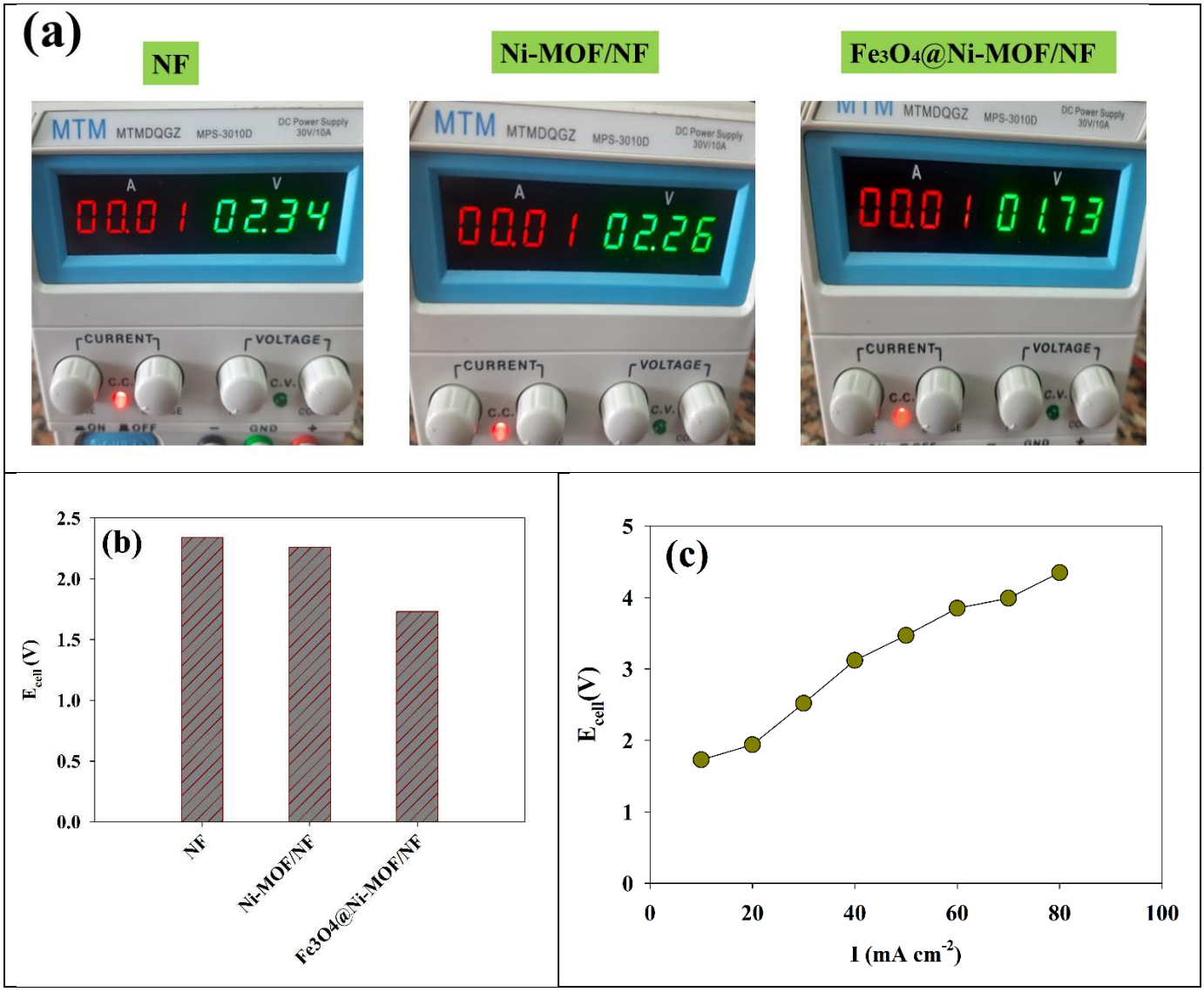


Figure 7. Electrochemical water-splitting performance: (a) raw constant-current data for the different modified electrodes, (b) comparison of cell voltage (E_{cell}) for the investigated electrodes, and (c) E_{cell} as a function of applied current for the Fe_3O_4@Ni-MOF/NF electrode.

Conclusion

In conclusion, the direct growth of hierarchical Fe_3O_4@Ni-MOF on nickel foam provides an effective strategy for constructing binder-free, multifunctional electrodes with integrated catalytic and energy-storage capabilities. The intimate coupling between the two components and the three-dimensional conductive framework creates a favorable electrode architecture that facilitates interfacial charge transfer, electrolyte penetration, and accessible electroactive sites. Beyond demonstrating activity in individual electrochemical processes, the successful operation of the electrode in a practical two-electrode water-splitting configuration highlights the potential of this architecture for translating laboratory-scale materials design into functional electrochemical systems. The combination of structural robustness, accessible porosity, and multifunctionality makes Fe_3O_4@Ni-MOF/NF a promising platform for developing integrated technologies for sustainable hydrogen production and energy storage.

Data availability statement

The datasets used and analyzed during the current study are available from the corresponding author upon reasonable request.

Conflict of Interest

The authors declare that there is no conflict of interest regarding the publication of this paper.

Author Contributions

Sameerah I. Al-Saeedi: Validation, Supervision, Resources, Project administration, Funding acquisition, Conceptualization. **Mahmoud A. Hefnawy:** Writing – original draft, Visualization, Validation, Methodology, Formal analysis, Data curation. **Ghadah M. Al-Senani:**Validation, Supervision, Resources, Project administration, Funding acquisition, Conceptualization. **Nada S. Al-Kadhi:** Validation, Supervision, Resources, Project administration, Funding acquisition, Conceptualization. **Hoda A. Ahmed**: Writing – review & editing, Supervision, Project administration, Methodology, Data curation, Conceptualization. **Shymaa S. Medany**: Writing – review & editing, Writing – original draft, Supervision, Software, Methodology, Investigation, Formal analysis, Data curation.

References:

[1] D.I. Stern, Energy and economic growth, in: Routledge Handb. Energy Econ., Routledge, 2019: pp. 28–46.

[2] K. Kaygusuz, Energy for sustainable development: key issues and challenges, Energy Sources, Part B Econ. Planning, Policy. 2 (2007) 73–83.

[3] D. Ahuja, M. Tatsutani, Sustainable energy for developing countries, SAPI EN. S. Surv. Perspect. Integr. Environ. Soc. (2009).

[4] S. Kumar, K. Rathore, Renewable energy for sustainable development goal of clean and affordable energy, Int. J. Mater. Manuf. Sustain. Technol. 2 (2023) 1–15.

[5] M. Höök, X. Tang, Depletion of fossil fuels and anthropogenic climate change—A review, Energy Policy. 52 (2013) 797–809.

[6] J.L. Holechek, H.M.E. Geli, M.N. Sawalhah, R. Valdez, A Global Assessment: Can Renewable Energy Replace Fossil Fuels by 2050?, Sustainability. 14 (2022). doi:10.3390/su14084792.

[7] Z.Q.S. Nwokediegwu, K.I. Ibekwe, V.I. Ilojianya, E.A. Etukudoh, O.B. Ayorinde, Renewable energy technologies in engineering: A review of current developments and future prospects, Eng. Sci. Technol. J. 5 (2024) 367–384.

[8] D. Gayen, R. Chatterjee, S. Roy, A review on environmental impacts of renewable energy for sustainable development, Int. J. Environ. Sci. Technol. 21 (2024) 5285–5310.

[9] N.L. Panwar, S.C. Kaushik, S. Kothari, Role of renewable energy sources in environmental protection: A review, Renew. Sustain. Energy Rev. 15 (2011) 1513–1524. doi:https://doi.org/10.1016/j.rser.2010.11.037.

[10] A. Elkhatat, S. Al-Muhtaseb, Climate change and energy security: a comparative analysis of the role of energy policies in advancing environmental sustainability, Energies. 17 (2024) 3179.

[11] M.J.B. Kabeyi, O.A. Olanrewaju, Sustainable energy transition for renewable and low carbon grid electricity generation and supply, Front. Energy Res. 9 (2022) 743114.

[12] P.-A. Le, V.D. Trung, P.L. Nguyen, T.V. Bac Phung, J. Natsuki, T. Natsuki, The current status of hydrogen energy: an overview, RSC Adv. 13 (2023) 28262–28287.

[13] S.O. Akpasi, I.M. Smarte Anekwe, E.K. Tetteh, U.O. Amune, S.I. Mustapha, S.L. Kiambi, Hydrogen as a clean energy carrier: advancements, challenges, and its role in a sustainable energy future, Clean Energy. 9 (2025) 52–88.

[14] B. Sundén, Hydrogen, batteries and fuel cells, Elsevier, 2019.

[15] J. Ohi, Hydrogen energy cycle: An overview, J. Mater. Res. 20 (2005) 3180–3187.

[16] B.N. Tackie-Otoo, M. Mahmoud, A. Raza, Renewable energy versus hydrogen energy: assessing current needs for sustainable energy solutions, Energy & Fuels. 39 (2025) 17730–17762.

[17] A. Alzahrani, S.K. Ramu, G. Devarajan, I. Vairavasundaram, S. Vairavasundaram, A review on hydrogen-based hybrid microgrid system: Topologies for hydrogen energy storage, integration, and energy management with solar and wind energy, Energies. 15 (2022) 7979.

[18] G.Z. Chen, Supercapacitor and supercapattery as emerging electrochemical energy stores, Int. Mater. Rev. 62 (2017) 173–202.

[19] J. Yan, Q. Wang, T. Wei, Z. Fan, Recent advances in design and fabrication of electrochemical supercapacitors with high energy densities, Adv. Energy Mater. 4 (2014) 1300816.

[20] B.K. Kim, S. Sy, A. Yu, J. Zhang, Electrochemical supercapacitors for energy storage and conversion, Handb. Clean Energy Syst. (2015) 1–25.

[21] K.O. Oyedotun, B.B. Mamba, New trends in supercapacitors applications, Inorg. Chem. Commun. 170 (2024) 113154.

[22] A.G. Olabi, Q. Abbas, A. Al Makky, M.A. Abdelkareem, Supercapacitors as next generation energy storage devices: Properties and applications, Energy. 248 (2022) 123617.

[23] Y. Zhao, L.P. Wang, M.T. Sougrati, Z. Feng, Y. Leconte, A. Fisher, M. Srinivasan, Z. Xu, A review on design strategies for carbon based metal oxides and sulfides nanocomposites for high performance Li and Na ion battery anodes, Adv. Energy Mater. 7 (2017) 1601424.

[24] G. Kothandam, G. Singh, X. Guan, J.M. Lee, K. Ramadass, S. Joseph, M. Benzigar, A. Karakoti, J. Yi, P. Kumar, Recent advances in carbon-based electrodes for energy storage and conversion, Adv. Sci. 10 (2023) 2301045.

[25] P. Simon, Y. Gogotsi, Materials for electrochemical capacitors, Nat. Mater. 7 (2008) 845–854.

[26] H. Gamal, A.M. Elshahawy, S.S. Medany, M.A. Hefnawy, M.S. Shalaby, Recent advances of vanadium oxides and their derivatives in supercapacitor applications: A comprehensive review, J. Energy Storage. 76 (2024) 109788. doi:https://doi.org/10.1016/j.est.2023.109788.

[27] V.F. Yusuf, N.I. Malek, S.K. Kailasa, Review on metal–organic framework classification, synthetic approaches, and influencing factors: applications in energy, drug delivery, and wastewater treatment, ACS Omega. 7 (2022) 44507.

[28] G. Cai, P. Yan, L. Zhang, H.-C. Zhou, H.-L. Jiang, Metal–organic framework-based hierarchically porous materials: synthesis and applications, Chem. Rev. 121 (2021) 12278–12326.

[29] S.D. Al-Qahtani, M.A. Hefnawy, G.M. Al-Senani, H.A. Ahmed, S.S. Medany, Three-dimensional Ni–Cr-MOF/CNT hybrid electrode on nickel foam for efficient water splitting and electrochemical capacitor applications, RSC Adv. (2026). doi:10.1039/d6ra05560e.

[30] G.M. Al-Senani, M.A. Hefnawy, H.A. Ahmed, S.S. Medany, Design of Ni-MOF/ZIF-67 hybrid catalyst for enhanced alkaline urea electrooxidation, Mater. Chem. Phys. 367 (2026) 133002. doi:https://doi.org/10.1016/j.matchemphys.2026.133002.

[31] G. John, T. Susikumar, M. Navaneethan, P. Justin Jesuraj, Intercalation of g-C3N4/Ag2S heterostructure on boronized Ni-MOF for enhanced water splitting and energy storage applications, Electrochim. Acta. 508 (2024) 145258. doi:https://doi.org/10.1016/j.electacta.2024.145258.

[32] S.S. Medany, M.A. Hefnawy, Applications of iron oxide-based supercapacitors, in: Green Sustain. Synth. Iron Oxide-Based Nanomater. Energy Environ. Appl., Elsevier, 2026: pp. 413–445.

[33] M.A. Hefnawy, S.S. Medany, R.M. El-Sherif, S.A. Fadlallah, Green synthesis of NiO/Fe3O4@chitosan composite catalyst based on graphite for urea electro-oxidation, Mater. Chem. Phys. 290 (2022) 126603. doi:https://doi.org/10.1016/j.matchemphys.2022.126603.

[34] H. Mishra, P. Sachan, M. Mandal, A. Yadav, S. Sunny, P.C. Mondal, Interface engineering between π-conjugated molecules and Fe_3O_4 nanoparticles for supercapacitors, J. Mater. Chem. C. (2026).

[35] E. Mazaheri, A. Gholizadeh, Hierarchical graphene oxide/Co-metal-organic framework/Fe_3O_4 structures for high-performance applications, J. Sol-Gel Sci. Technol. 119 (2026) 29.

[36] S.D. Al-Qahtani, M.A. Hefnawy, G.M. Al-Senani, F.F. Al-Fawzan, H.A. Ahmed, R.A. Alahmari, S.S. Medany, Facile Design of Fe3O4/Fe-MOF@RGO Hybrid Nanocomposites for Efficient

Electrocatalytic Water Splitting and High-Performance Supercapacitors, J. Inorg. Organomet. Polym. Mater. (2026). doi:10.1007/s10904-026-04490-8.

[37] E.A. Namikuchi, R.D.L. Gaspar, D.S. da Silva, I.M. Raimundo, I.O. Mazali, PEG size effect and its interaction with Fe3O4 nanoparticles synthesized by solvothermal method: morphology and effect of pH on the stability, Nano Express. 2 (2021) 20022. doi:10.1088/2632-959X/ac0596.

[38] A. Pathak, K. Hatakeyama, S. Ida, Morphology Control of Two dimensional (2D) Metal–Organic Framework Nanosheets via 1 nm Thick Hexagonal Hydroxide Nanosheets through Variable Reaction Parameters, Adv. Mater. Interfaces. 10 (2023) 2300335. doi:https://doi.org/10.1002/admi.202300335.

[39] D. Zhu, J. Liu, Y. Zhao, Y. Zheng, S.-Z. Qiao, Engineering 2D Metal–Organic Framework/MoS2 Interface for Enhanced Alkaline Hydrogen Evolution, Small. 15 (2019) 1805511. doi:https://doi.org/10.1002/smll.201805511.

[40] C.A. Downes, A.J. Clough, K. Chen, J.W. Yoo, S.C. Marinescu, Evaluation of the H2 Evolving Activity of Benzenehexathiolate Coordination Frameworks and the Effect of Film Thickness on H2 Production, ACS Appl. Mater. Interfaces. 10 (2018) 1719–1727. doi:10.1021/acsami.7b15969.

[41] F.S. Alamro, M.A. Hefnawy, N.S. Al-Kadhi, R. AL-Faze, H.A. Ahmed, S.S. Medany, Synergistic effect of CuO and polyaminoanthraquinone on water splitting kinetics, Int. J. Hydrogen Energy. 186 (2025) 151886. doi:https://doi.org/10.1016/j.ijhydene.2025.151886.

[42] W. Cheng, H. Zhang, D. Luan, X.W. Lou, Exposing unsaturated Cu1-O2 sites in nanoscale Cu-MOF for efficient electrocatalytic hydrogen evolution, Sci. Adv. 7 (2021) eabg2580.

[43] S.D. Al-Qahtani, M.A. Hefnawy, G.M. Al-Senani, F.F. Al-Fawzan, H.A. Ahmed, D.J. Saleh, S.S. Medany, Engineering ZnMnCoO4@Polyaniline nanowire hybrid electrodes for alkaline HER/OER electrocatalysis and durable supercapacitor performance, RSC Adv. (2026). doi:10.1039/d6ra05105g.

[44] J. Duan, S. Chen, C. Zhao, Ultrathin metal-organic framework array for efficient electrocatalytic water splitting, Nat. Commun. 8 (2017) 15341. doi:10.1038/ncomms15341.

[45] P. Thangavel, M. Ha, S. Kumaraguru, A. Meena, A.N. Singh, A.M. Harzandi, K.S. Kim,

Graphene-nanoplatelets-supported NiFe-MOF: high-efficiency and ultra-stable oxygen electrodes for sustained alkaline anion exchange membrane water electrolysis, Energy Environ. Sci. 13 (2020) 3447–3458. doi:10.1039/D0EE00877J.

[46] S.D. Al-Qahtani, M.A. Hefnawy, G.M. Al-Senani, H.A. Ahmed, S.S. Medany, Design of Ag-modified Ni/Cr-MOF/carbon felt electrode for dual energy conversion and storage applications, RSC Adv. (2026). doi:10.1039/d6ra06163j.

[47] L. Sondermann, W. Jiang, M. Shviro, A. Spieß, D. Woschko, L. Rademacher, C. Janiak, Nickel-Based Metal-Organic Frameworks as Electrocatalysts for the Oxygen Evolution Reaction (OER), Molecules. 27 (2022) 1241. doi:10.3390/molecules27041241.

Supplementary Files

This is a list of supplementary files associated with this preprint. Click to download.

- supplementver4.0.docx